Eng. Sci., 2025, **33**, 1330

Engineered Science
DOI: https://dx.doi.org/10.30919/es1330

A Study on the Effect of Doping Silver Nanowires on the Spectral Properties of Cesium Tungsten Bronze Thin Films

Siyang Zhang,[1, 2] Zeming He,[1,*] Ming Yang,[1, 2] Zeinhom M. El-Bahy,[3] Aricson Pereira[4] and Hang Zhang[1, 2,*]

Abstract

The study investigates AgNWs (Silver nanowires)-doped $Cs_{0.32}WO_3$ films as a year-round energy-saving solution in comparison with ordinary glass and $Cs_{0.32}WO_3$ films. The article indicates that although $Cs_{0.32}WO_3$ provides superior solar radiation blocking compared to traditional materials, its performance is not up to par throughout the year due to high photothermal conversion and emissivity. Doping the films with AgNWs, with their low emissivity and high mid-far infrared reflectance, addresses this limitation. Approximately 98% of solar radiation falls within the range of 200 nm ~ 2500 nm band, in which the near-infrared (NIR) light in the band of 780 nm ~ 2500 nm constitutes 51% of this spectrum, while 96% of the thermal radiation of normal objects is concentrated within the mid-far infrared (MIR) band of 2.5 μm ~ 25 μm. Ordinary glass, with a thickness of 3 mm, exhibits a remarkable transmittance of 90% within the solar radiation spectrum, which will increase the energy consumption of cooling in summer months, while the absorbance in the mid-far infrared band reaches up to 88.1%, which will increase the heating energy consumption during winter. Based on the characteristics of intrinsic absorption, local surface plasmon resonance (LSPR), and small polaron absorption, cesium tungsten bronze (Cs_xWO_3) exhibits a superior capacity to block solar radiation than tin oxide and other tungsten bronze materials. However, Cs_xWO_3 film has an obvious photothermal conversion efficiency and a high emissivity, which will cause a strong radiation heat exchange with the indoor environment in summer and winter. AgNWs have low emissivity and high mid-far infrared reflectance owing to their dense network structure, effectively mitigating the radiation heat exchange. In this paper, solid-state reaction method, ball milling, and centrifugation were used to prepare nano $Cs_{0.32}WO_3$ slurries (particle size is < 50 nm), then at T_{550nm} = 70% and T_{550nm} = 60%, eight samples of non-doped $Cs_{0.32}WO_3$ films, $Cs_{0.32}WO_3$ films doped with AgNWs, Low-E films, and double-sided coating films were prepared respectively to carry out the performance testing experiments. By simulating indoor heating in winter and indoor warming in summer, the experiments demonstrate that at a certain T_{550nm}, for example, T_{550nm} = 60%, the $Cs_{0.32}WO_3$ thin film doped with AgNWs can possess robust solar radiation blocking ability (B_{1400nm} > 94%), low emissivity (ε_{surf} < 0.35) and high mid-far infrared reflectance (R_{MIR} > 65%), achieve a good energy saving effect both in winter and summer, effectively make up for the shortcoming of the non-doped $Cs_{0.32}WO_3$ films which show an inferior energy-saving performance during winter, and provide meaningful technical reference and data support for further optimization of $Cs_{0.32}WO_3$ thin film properties.

Keywords: Cesium tungsten bronze; Silver nanowires; Near-infrared blocking; Energy saving.
Received: 26 April 2024; Revised: 22 June 2024; Accepted: 07 July 2024.
Article type: Research article.

1. Introduction

Windows are the most energy-consuming part of the building envelope,[1] and have been an important link in the research and design of building energy conservation. Studies have shown that the energy consumption of the window is mainly caused by thermal radiation.[2] In order to regulate the radiation characteristics of glass, we need first to understand the difference between the solar radiation and normal objects' radiation. As shown in Fig. 1, 98% of solar radiation is distributed in the 200 nm ~ 2500 nm band, of which the ultraviolet (UV) light in the band of 200 nm ~ 380 nm accounts for 3%, the visible light in the band of 380 nm ~ 780 nm accounts for 44%, and the near-infrared (NIR) light in the band of 780 nm ~ 2500 nm accounts for 51%.[3] In nature, 96% of the thermal radiation of normal objects is distributed in the mid-far infrared (MIR) band of 2.5 μm ~ 25 μm. This difference provides a theoretical basis for regulating glass

[1] *Institute of Engineering Thermophysics, Chinese Academy of Sciences, Beijing 100190, China.*

radiation.

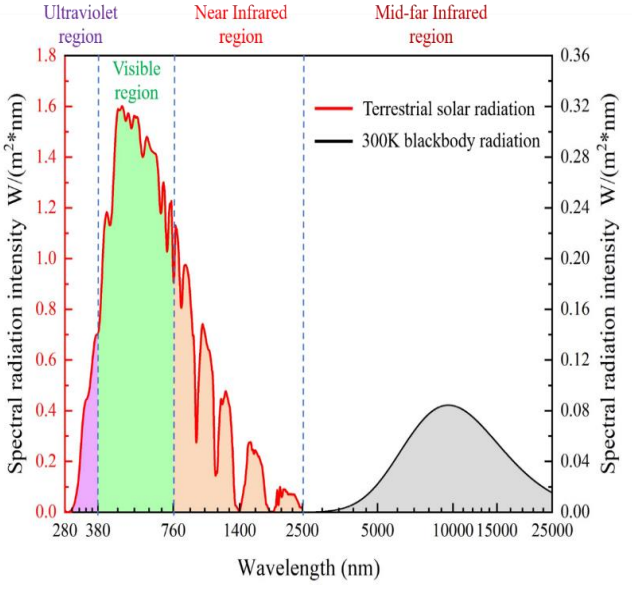

Fig. 1 The difference between the solar radiation and 300K blackbody's radiation.

The spectral properties of glass also need to be understood. As shown in Fig. 2, the transmittance of 3 mm thick ordinary glass in the solar radiation band is as high as 90%, while the absorbance in the mid-far infrared band is as high as 88.1%. Under cooling conditions in summer, a lot of solar radiation gets through the ordinary glass, causing the indoor temperature to rise, while the mid-far infrared thermal radiation of outdoor higher-temperature objects is absorbed a lot by ordinary glass, which transfers heat to the room, both ways will increase the energy consumption of refrigeration. Under heating conditions in winter, ordinary glass absorbs a lot of the thermal radiation from indoor higher-temperature objects, then dissipates heat to the outside in a large amount, and consequently increases the heating energy consumption, as shown in Fig. 3. This is the key for glass to become the main part of building energy consumption.[4]

If the glass can maintain a high transmittance in the 380 nm ~ 760 nm band, meeting the need of indoor daylighting, block the solar radiation into the room in summer and reduce the absorbance of thermal radiation from indoor higher-temperature objects in winter, it can effectively reduce indoor energy consumption both in winter and summer. This is the focus of research on glass energy-saving.

Based on the characteristics of intrinsic absorption,[5] local surface plasmon resonance (LSPR),[6] and small polaron absorption,[7] tungsten bronze (M_xWO_3) has a stronger solar radiation blocking ability compared to tin oxide, such as ITO (Indium Tin Oxide),[8] ATO (Antimony Tin Oxide),[9] FTO (Fluorine-doped Tin Oxide),[10] as well as other thermal insulation materials. This makes it more effective in shielding solar near-infrared radiation.[11] In the tungsten bronze family, each Cs^+ of cesium tungsten bronze (Cs_xWO_3) can provide the most 0.96 electrons,[12] which makes Cs_xWO_3 possess the strongest infrared shielding ability—more than 70% transmittance at 550 nm and more than 95% blocking rate at 1400 nm.[13] In addition, Cs_xWO_3 has the advantages of low price and easy preparation, which make it the first choice for the new generation of energy-saving films.[14]

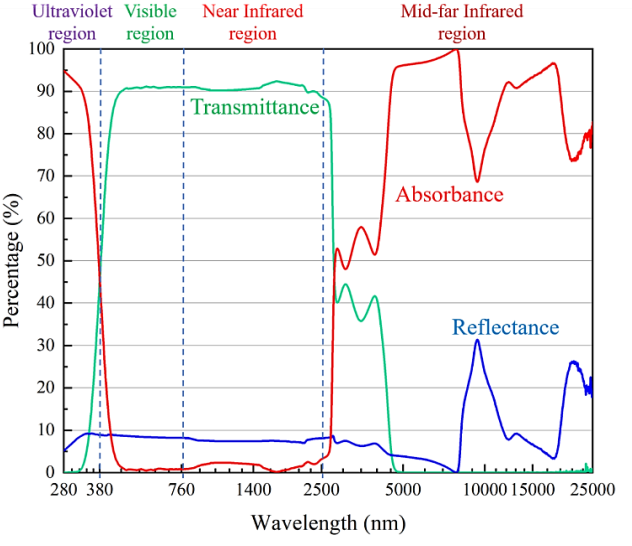

Fig. 2 The spectral characteristic curves of 3mm thick ordinary glass.

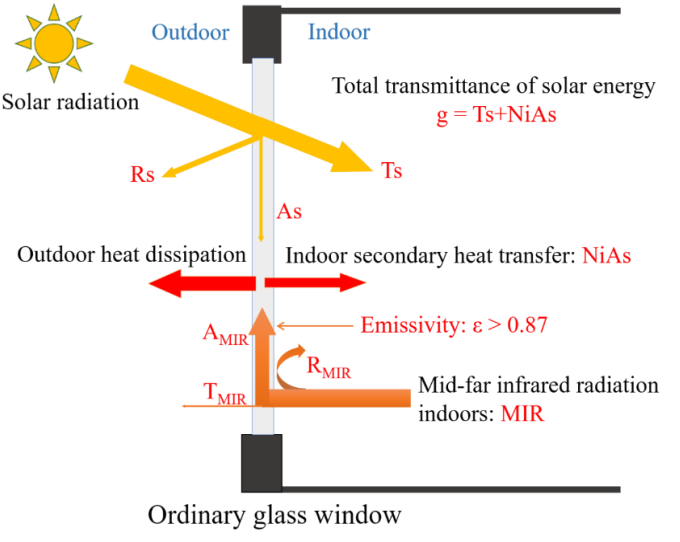

Fig. 3 The schematic diagram of spectral characteristics of ordinary glass.

[2] *University of Chinese Academy of Sciences, Beijing 100049, China.*
[3] *Department of Chemistry, Faculty of Science, Al-Azhar University, Nasr City, Cairo 11884, Egypt.*
[4] *Engineered Multifunctional Composites (EMC) Nanotech LLC, Knoxville, TN, 37996, United States.*
**Email:* zhanghang@iet.cn (Z. Hang); hezeming@iet.cn (H. Zeming)

The performance of cesium tungsten bronze is closely related to the crystalline structure and particle size, and its solar radiation blocking performance will obviously improve when the nanoparticle size is less than 50 nm.[15] At present, the principal preparation methods include the solid-state reaction method, the hydrothermal method, and the solvothermal method.[16] The solid-state reaction method has the simplest principle: the raw materials are mixed according to the atomic ratio of the expected product, the mixture is calcined at a high temperature for a certain time, and then the expected product can be obtained. Raw materials are typically tungstic acid, ammonium tungstate, and cesium carbonate, which are inexpensive and readily available. Moreover, the cost of the required equipment and process is not exorbitant. Therefore, the solid-state reaction method is more suitable for mass production.[17] However, the low migration rate of the solid-phase components will lead to uneven doping, and the product topography is uncontrollable. Additionally, the high temperature sintering will increase the size of Cs_xWO_3 particles, mostly sub-micron particles, which should be put into application only after secondary ball milling treatment.[18] The reagent thermal method and hydrothermal method generally use tungstic acid, cesium hydroxide, or cesium carbonate as raw materials to nucleate and crystallize in oxalic acid, citric acid, and other acidic solutions at a high temperature and pressure and can directly generate nanorod crystal structure and reduce agglomeration phenomenon, which is beneficial to subsequent treatment and application.[19] However, these two liquid-phase methods require high purification equipment, long reaction times, and strict reaction conditions, which cannot be adjusted once produced. Moreover, the nanorod morphology will weaken its near-infrared blocking properties to a certain extent and also affect the stability of the prepared cesium-tungsten bronze slurry and the permeability and fog of the coating film.[20] Therefore, the appearance of long rod-shaped Cs_xWO_3 nanocrystals should be avoided in the Cs_xWO_3 slurry.

However, Cs_xWO_3 has an obvious photothermal conversion efficiency (73%),[21] when applied to the inner surface of the glass window, as shown in Fig. 4, the Cs_xWO_3 film will absorb a large amount of solar infrared radiation and mid-far infrared radiation in summer, resulting in a rise in room temperature, and its emissivity is as high as 0.87 or more, which causes a strong radiation heat exchange with indoor environment in summer or winter, so its heat insulation and energy saving performance needs to be improved.

Silver is the precious metal with the strongest electrical conductivity and has the advantages of high thermal conductivity, high ductility, high plasticity, etc. When the particle size of silver is below 50 nm, it begins to have obvious characteristics such as small size effect, surface effect, quantum size effect, and macroscopic quantum tunneling effect. Experiments show that silver nanowires (AgNWs) have low emissivity and high infrared reflectance.[22] The diameter of AgNWs is generally 15 nm ~ 70 nm, and the length is several microns to tens of microns, and the dense network structure can be formed at a certain concentration of AgNWs (the gap is less than 300 nm).[23] As shown in Fig. 5, the network structure of this nanoscale spacing is equivalent to an "impenetrable wall", which can reflect most of the mid-far infrared radiation. When applied to the inner surface of the glass window (Fig. 6), the surface emissivity of the Cs_xWO_3 film is reduced by doping AgNWs, which can reduce the radiation heat exchange of the glass window with the room in summer and increase the mid-far infrared reflectance in winter. Thus, doping AgNWs can effectively make up for the

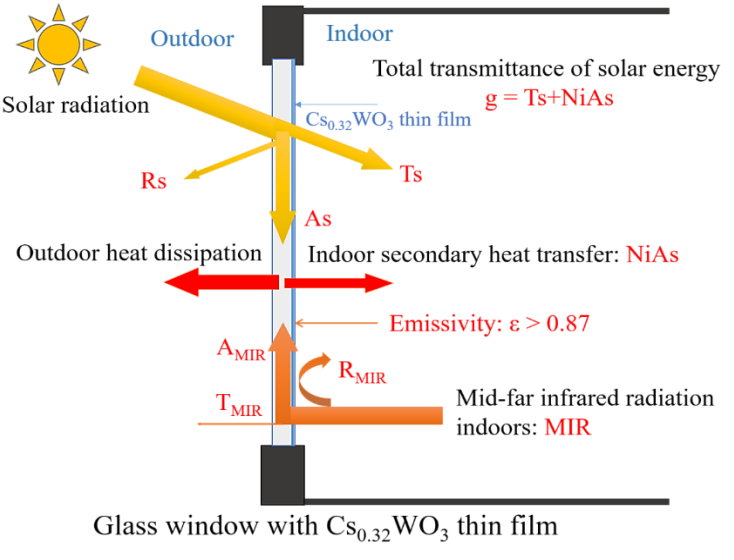

Fig. 4 The schematic diagram of spectral characteristics of $Cs_{0.32}WO_3$ thin film.

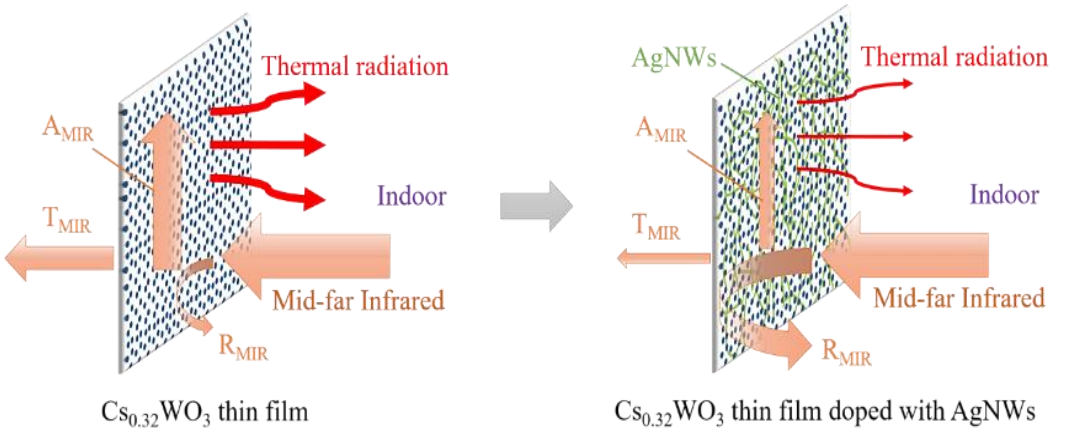

Fig. 5 The functional diagram of AgNWs.

shortcoming of high emissivity of Cs_xWO_3 films.

A single thermal insulation functional material takes effect only in a certain wavelength band, in order to prepare a coating with excellent comprehensive insulation function, two or more thermal insulation mechanisms need to be integrated,[24] that is, a variety of thermal insulation materials need to be mixed for performance analysis and optimization. In this paper, nano-$Cs_{0.32}WO_3$ ball-milled slurry and AgNWs slurry were mixed, and the effect of doping AgNWs on the spectral properties of $Cs_{0.32}WO_3$ thin films was studied by spectral analysis and experimental verification. Finally, a $Cs_{0.32}WO_3$ thin film doped with AgNWs, which can significantly reduce the surface emissivity, improve the mid-far infrared reflectance and maintain a high solar blocking property, has been determined.

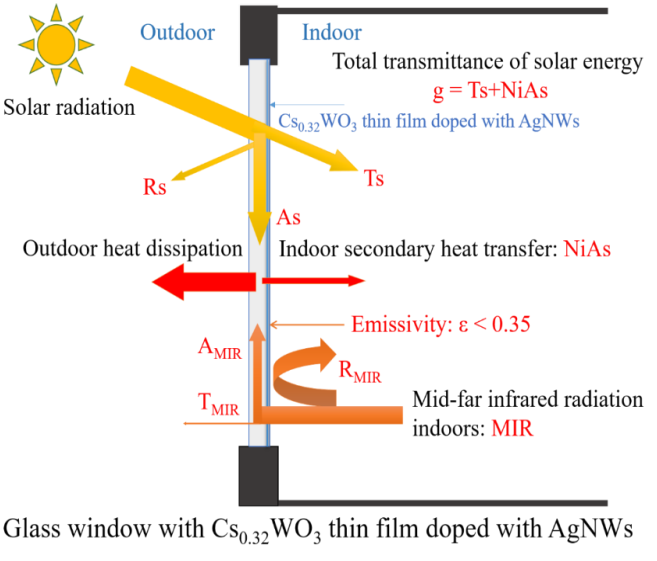

Fig. 6 The schematic diagram of spectral characteristics of $Cs_{0.32}WO_3$ thin film doped with AgNWs.

2. Experimental process

The experimental process of this paper is shown in Fig. 7. Firstly, $Cs_{0.32}WO_3$ powder was prepared using the solid-state reaction method. After premixing and drying of ammonium metatungstate (AMT) and cesium carbonate (Cs_2CO_3) raw materials, the optimum preparation parameters of temperature and gas flow rate were determined by comparing the X-Ray Diffraction (XRD) pattern of standard cesium tungsten bronze with the $Cs_{0.32}WO_3$ powder prepared in different conditions of heating temperature and flow rate of the reduction gas. Then, uniformly dispersed nano $Cs_{0.32}WO_3$ slurries were prepared by ball milling for 48 hours and centrifugation for 40 minutes of the premixed $Cs_{0.32}WO_3$ dispersion liquid. The nano $Cs_{0.32}WO_3$ particle size was less than 50 nm. Subsequently, eight thin film samples were prepared using the machine coating method with varying configurations: $Cs_{0.32}WO_3$ films doped with 1 wt.% AgNWs, low emissivity films, double-sided coating films, and undoped $Cs_{0.32}WO_3$ films as the baseline under the conditions of T_{550nm} = 70% and T_{550nm} = 60% visible light transmittance to conduct the glass hut experiments. Finally, by simulating indoor heating in winter (dry, clear, and windless, temperature range: -4 ℃ ~ 5 ℃) and indoor warming in summer (dry, clear, and windless, time range: 1 pm ~ 3 pm, outdoor temperature: 8 ℃), the comprehensive energy-saving effect of $Cs_{0.32}WO_3$ thin films doped with AgNWs were verified.

3. Results and discussion

3.1 Preparation and characterization of $Cs_{0.32}WO_3$ powder

First, 27.3 g of ammonium metatungstate (AMT) and 6 g of cesium carbonate (Cs_2CO_3) are weighed according to the molar ratio of 1:3 and then mixed with 40 g of ethanol. After being premixed by magnetic stirring for 30 minutes, the mixture liquid is put into a beaker and dried in a vacuum drying oven at 40 ℃ for 12 hours to form a white coarse powder. Then grind the coarse powder for 5 minutes and sieve it through a 400-mesh number screen to form a white fine powder, as shown in Fig. 8.

Because AMT will be pyrolyzed to tungsten trioxide above 600 ℃,[25] then cesium ions can enter the crystalline vacancy of tungsten bronze, so the heating temperature is initially set at 650 ℃. Put 10 g of white fine powder into the crucible and send it into the high-temperature tube furnace. First, under 200 sccm flow rate of the H_2(20%)/Ar Reducing

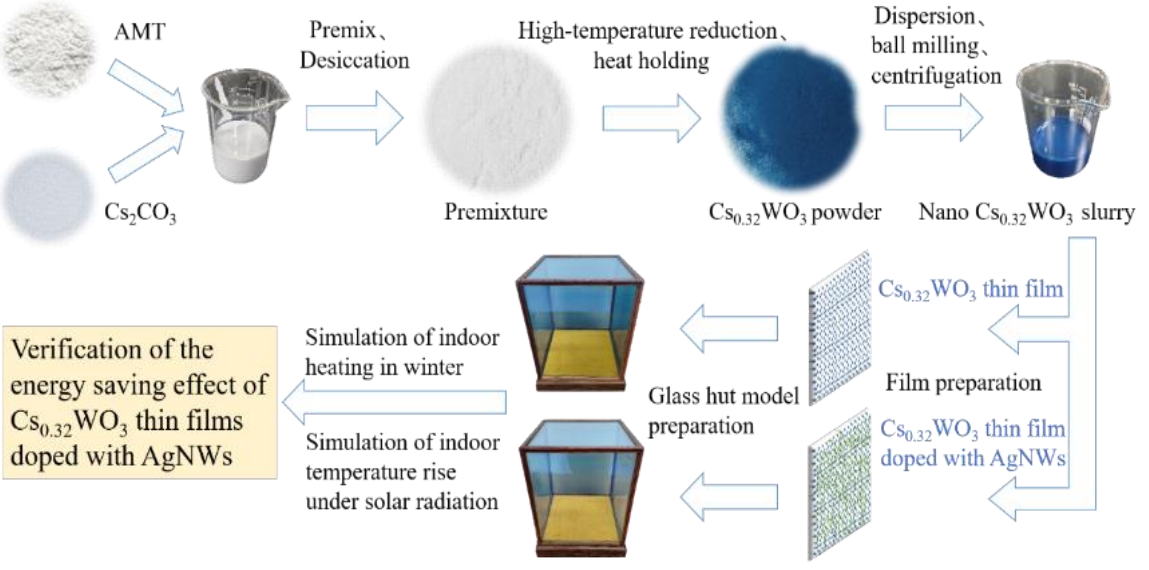

Fig. 7 The experimental flow chart.

gas mixture, the heating rate is set at 10 ℃/min, then heat the powder at 650 ℃, 700 ℃, 750 ℃ and 800 ℃ respectively for 1.5 hours. Subsequently turn off the H_2(20%)/Ar air source and hold the same temperature for 1.5 hours. After cooling the powder naturally to normal temperature, take out the powder and grind it in mortar by dust-free cloth for 5 minutes, then sieve it through the 400-mesh number screen to form the final powder products shown in Fig. 8. At 650 ℃, the powder is grayish-blue, as shown in Fig. 8(a); with the increase of heating temperature, the powder color gradually becomes darker, and it is already dark blue at 750 ℃, as shown in Fig. 8(c); but when the heating temperature rises to 800 ℃, the powder color becomes dark grayish-blue, as shown in Fig. 8(d). It is possible that the structure of cesium-tungsten bronze changes under this condition.

The cesium tungsten bronze powder prepared at 200 sccm gas flow rate was scanned by scanning electron microscope (SEM), as shown in Fig. 9. When the heating temperature is 650 ℃, the crystalline particles start to generate a lot but irregularly, there are many small particles that do not react, as shown in Fig. 9 (a). When the heating temperature is 700 ℃, the crystalline particles increase significantly, and the regular morphology begins to appear, as shown in Fig. 9(b). When the heating temperature is 750 ℃, there is an uneven rod-like structure with a diameter between 100 nm and 200 nm and a length between 100 nm and 400 nm. At this time, the reaction is sufficient, but there are still a few fine particles, as shown in Fig. 9(c). However, when the heating temperature is 800 ℃, a large laminated structure appears, the powder's hardness increases significantly, and no small particles remain, indicating that the reaction is complete and the crystal phase changes, as shown in Fig. 9(d). XRD analysis can confirm the hypothesis of crystal phase change.

The crystallinity of the Cs_xWO_3 powder prepared at 200 sccm gas flow rate was analyzed by XRD, and the results are shown in Fig. 10. It can be seen that when the heating temperature is 650 ℃ ~ 800 ℃, the positions of diffraction peaks at 2Θ are completely consistent with the standard $Cs_{0.32}WO_3$ (The XRD diffraction peaks of standard $Cs_{0.32}WO_3$ is JCPDS NO.83-1334). With the increase of temperature, the intensity of diffraction peaks continues to rise, and reaches the highest value at 750 ℃, and decreases significantly at 800 ℃, indicating that the crystallization degree of the powder sample prepared at 750 ℃ is basically consistent with the standard $Cs_{0.32}WO_3$.

After determining the heating temperature as 750 ℃, a certain amount of prepared white fine powder was put into the crucible and sent into the high-temperature tube furnace. The

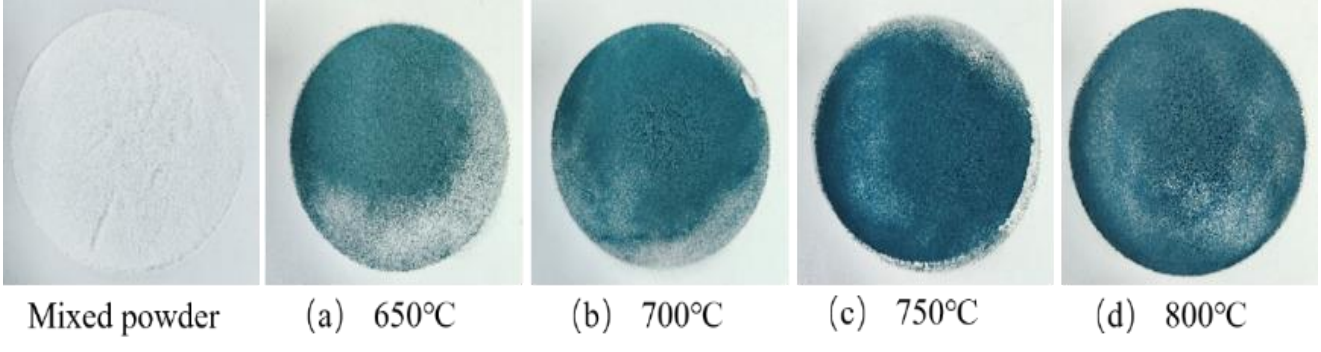

Fig. 8 The Cs_xWO_3 powder prepared at different heating temperature in 200 sccm H_2(20%)/Ar.

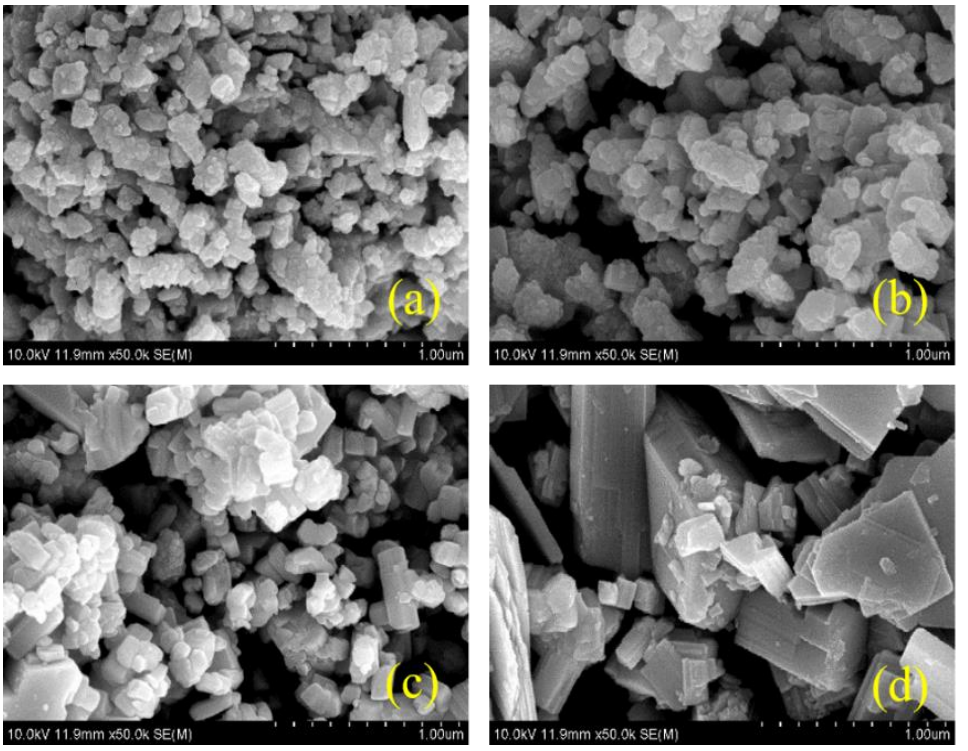

Fig. 9 The SEM images of Cs_xWO_3 powder prepared at different heating temperature in 200 sccm H_2(20%)/Ar.

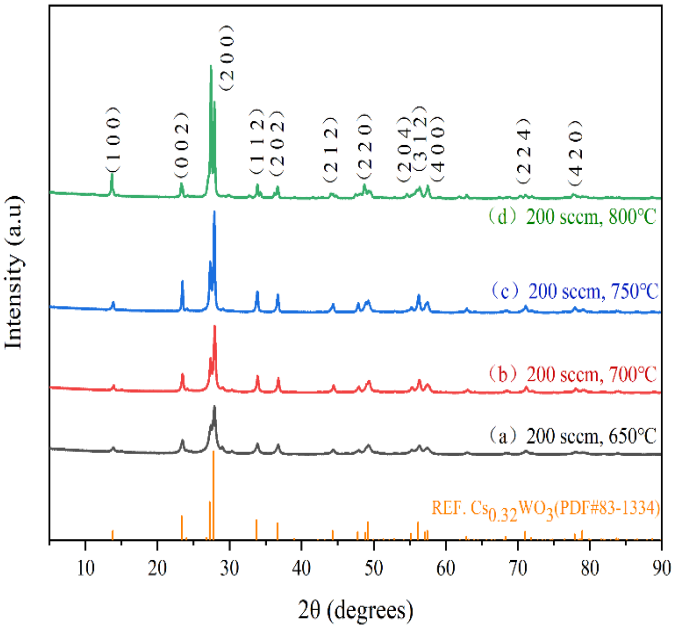

Fig. 10 The XRD pattern of Cs_xWO_3 powder prepared at different heating temperature in 200 sccm H_2(20%)/Ar.

heating rate was set at 10 ℃/min, and the flow rate of H_2 (20%)/Ar reducing gas mixture was set at 200 sccm, 300 sccm, 400 sccm and 500 sccm respectively, then heat the powder at 750 ℃ for 1.5 hours. Subsequently, the H_2 (20%)/Ar air source should be turned off and the temperature should be the same for 1.5 hours. After cooling the powder naturally to normal temperature, take it out and grind it for 5 minutes, then sieve it through the 400-mesh number screen to form the final powder products shown in Fig. 11.

When the H_2(20%)/Ar gas flow rate is 200 sccm, the powder color is dark blue. With the increase of H_2(20%)/Ar gas flow rate, the luster of $Cs_{0.32}WO_3$ powder gradually increases, and the color becomes more pure, as shown in Figs. 11(b)-(c). When the H_2(20%)/Ar gas flow rate reaches the maximum of 500 sccm, the luster of the cesium tungsten bronze powder is obvious, and the color becomes pure, as shown in Fig. 11(d). This provides a good understanding of the effect of H_2(20%)/Ar gas flow rate on $Cs_{0.32}WO_3$ powder characteristics.

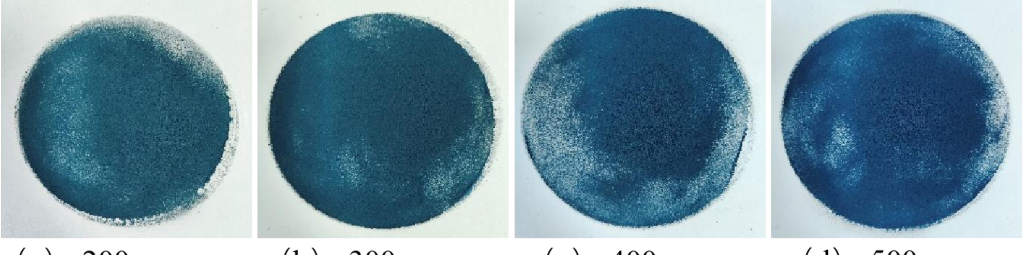

Fig. 11 The $Cs_{0.32}WO_3$ powder prepared at different flow rates of H_2(20%)/Ar at 750 ℃ heating temperature.

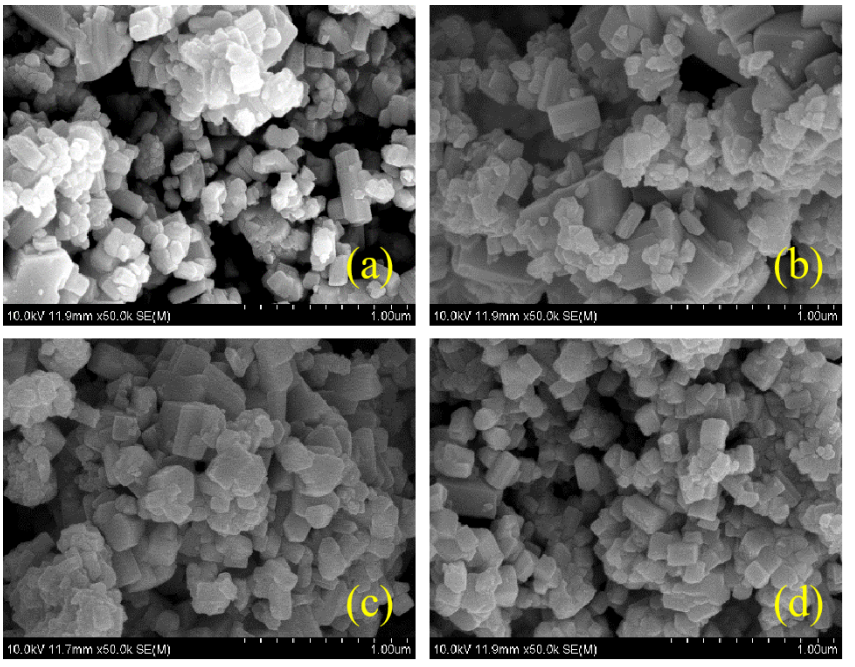

Fig. 12 The SEM images of $Cs_{0.32}WO_3$ powder prepared at different flow rates of H_2(20%)/Ar at 750 ℃ heating temperature.

The $Cs_{0.32}WO_3$ powder prepared above was further scanned by SEM, and the results were shown in Fig. 12. When the H_2(20%)/Ar gas flow rate is 200 sccm, the particle morphology is uneven rod-like structure, with the particle size ranging from 100 nm to 200 nm and the length from 100 nm to 400 nm, as shown in Fig. 12(a). In this case, the crystallization rate is faster, but there are still a few fine particles, and the reaction is still insufficient. When the H_2(20%)/Ar gas flow rate is 300 cm, the rod-like structure rapidly increases, but the heterogeneity increases, as shown in Fig. 12(b), indicating that the crystallization rate is accelerated but still uneven. When the H_2(20%)/Ar gas flow rate is 400 sccm, the particle morphology becomes uniform, as shown in Fig. 12(c), and the particle size ranges from 100 nm to 200 nm, and the length ranges from 100 nm to 300 nm. When the H_2(20%)/Ar gas flow rate reaches 500 sccm, the rod-like structure of the particles is clear, as shown in Fig. 12(d), and the size is significantly reduced and most uniform. The particle size is nearly between 100 nm and 150 nm, and the length is between 100 nm and 200 nm. Under this condition, the crystallization is most uniform and adequate.

The crystallinity of the $Cs_{0.32}WO_3$ powder prepared at different gas flow rates at 750 ℃ was analyzed by XRD, and the results are shown in Fig. 13. It can be seen that the positions of powder diffraction peaks prepared at each gas flow rate are completely consistent with that of the standard $Cs_{0.32}WO_3$ (PDF#83-1334). when the heating temperature is 750 ℃, with the increase of H_2(20%)/Ar gas flow rate, the diffraction peak intensity continues to rise. When the gas flow rate reaches 500sccm, the diffraction peaks' intensity reaches the highest value. It can be concluded that the crystallization degree of aforementioned $Cs_{0.32}WO_3$ powder prepared at 500 sccm H_2(20%)/Ar gas flow rate at 750 ℃ is closest to the standard $Cs_{0.32}WO_3$.

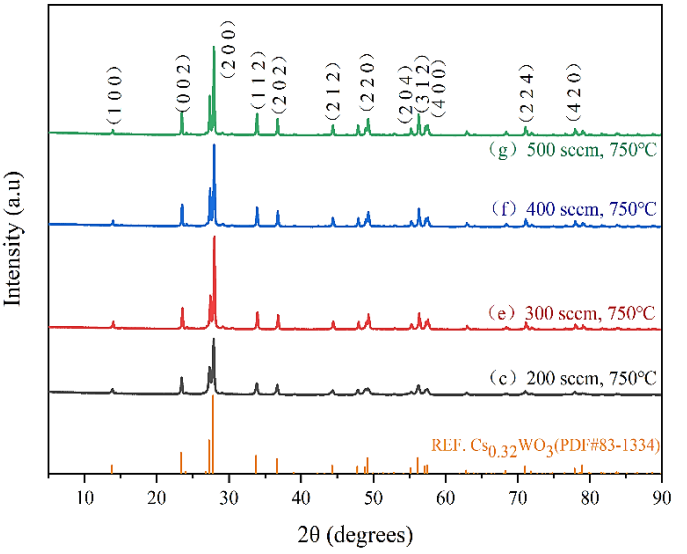

Fig. 13 The XRD pattern of $Cs_{0.32}WO_3$ powder prepared at different flow rates of H_2(20%)/Ar at 750 ℃ heating temperature.

This suggests $Cs_{0.32}WO_3$ powder can be successfully synthesized, to achieve optimal properties of uniform particle morphology and crystallinity by heating temperature of 750 ℃ and H_2(20%)/Ar gas flow rate of 500 sccm.

3.2. Preparation and characterization of nano $Cs_{0.32}WO_3$ slurries

First, use an electronic balance to weigh the prepared

$Cs_{0.32}WO_3$ powder 2.5 g, PVP 7.5 g, dispersant 0.5 g and solvent 39.5 g. After being premixed by magnetic stirring for 30 minutes, dispersion liquid containing 5 wt.% $Cs_{0.32}WO_3$ can be obtained. Through ball milling at 700 r/min for 48 hours, the $Cs_{0.32}WO_3$ slurry is then centrifuged at 1000 r/min for 20 minutes, 40 minutes and 60 minutes respectively, take out the upper layer of the $Cs_{0.32}WO_3$ slurry, wash it fully with deionized water, centrifuge it at 2000 r/min for 30 minutes, and dry it at 60 ℃ in a vacuum drying oven for 12 hours to precipitate a solid $Cs_{0.32}WO_3$ layer. Subsequently, the aforementioned process was repeated three times to ultimately obtain four types of nano $Cs_{0.32}WO_3$ powder. Subsequently, the powder was scanned by SEM, and the results are presented in Fig. 14.

In the absence of centrifugal treatment, the particle size distribution of $Cs_{0.32}WO_3$ in the ball milling liquid was relatively wide, mostly ranging from 40 nm to 70 nm, and a small number of particles exceeding 70 nm, as shown in Fig. 14(a). After centrifugation for 20 minutes, most particles' size was basically around 50 nm, and no size over 70 nm was found, as shown in Fig. 14(b). After centrifugation for 40 minutes, the particle size further decreased, almost distributing in the range from 40 nm to 50 nm, as shown in Fig. 14(c). After centrifugation for 60 minutes, the particle size distribution was nearly the same as that after centrifugation for 40 minutes, as shown in Fig. 14(d). It can be seen that when centrifugation is more than 40 minutes, the particle size of $Cs_{0.32}WO_3$ in the ball milling slurry is below 50 nm, which meets the experimental requirement about nano $Cs_{0.32}WO_3$ particle size.

3.3 Preparation and characterization of $Cs_{0.32}WO_3$ thin films

Firstly, six different $Cs_{0.32}WO_3$ dispersion liquids were prepared respectively according to the $Cs_{0.32}WO_3$ content of 5 wt.%, 10 wt.%, 15 wt.%, 20 wt.%, 25 wt.% and 30 wt.%. After being premixed by magnetic stirring for 30 minutes, ball milling at 700 r/min for 48 hours, centrifuging at 1000 r/min for 40 minutes, every $Cs_{0.32}WO_3$ dispersion slurry was added with 2 wt.% nano-silicone resin and magnetically-stirred for 20 minutes. Then coated every $Cs_{0.32}WO_3$ dispersion slurry on Polyethylene Terephthalate (PET) film with a coating machine (thickness set at 30μm), heated $Cs_{0.32}WO_3$ thin films at 70 ℃ for 10 minutes, then numbered these films as C5, C10, C15, C20, C25, C30 in accordance with the $Cs_{0.32}WO_3$ content in the slurry, and finally retained them for inspection.

The surface emissivity (ε_{surf}) of C5 ~ C30 film samples was measured by infrared images from the Fortric infrared imager. As shown in Fig. S1, all samples ε_{surf} were above 0.88. It can be seen that the content of $Cs_{0.32}WO_3$ in the slurries basically does not affect the characteristic of high emissivity of the $Cs_{0.32}WO_3$ thin films, while the color of the six films change from light blue to dark blue.

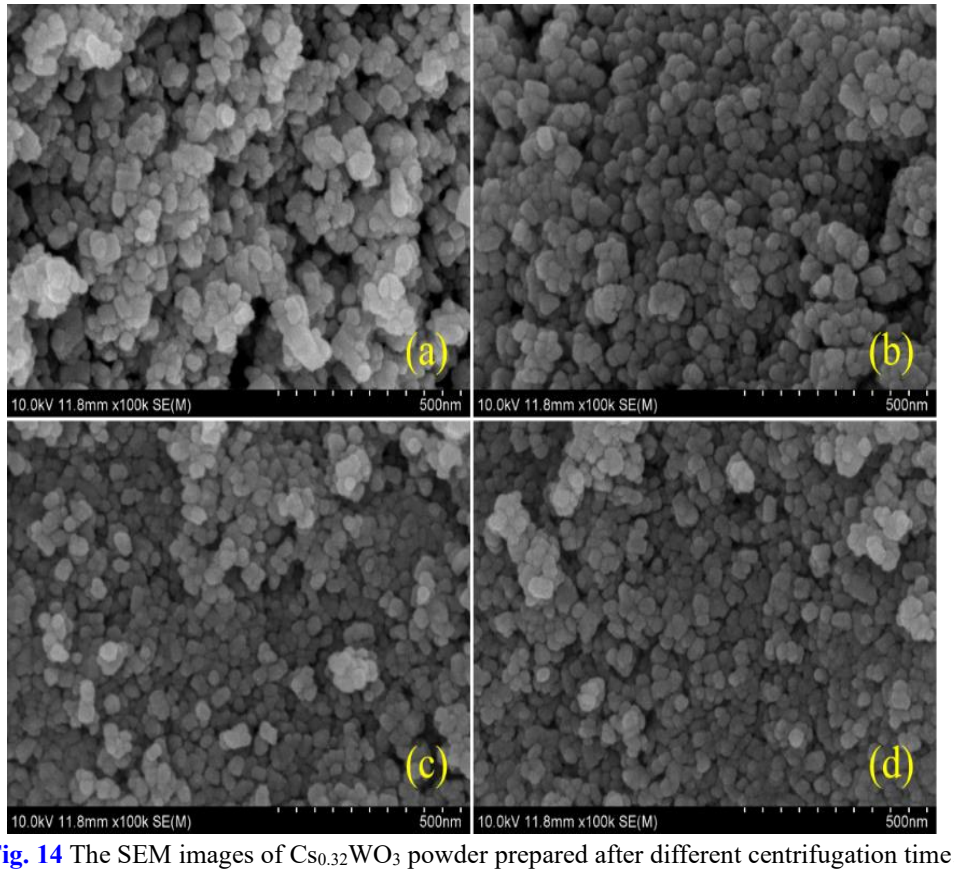

Fig. 14 The SEM images of $Cs_{0.32}WO_3$ powder prepared after different centrifugation time.

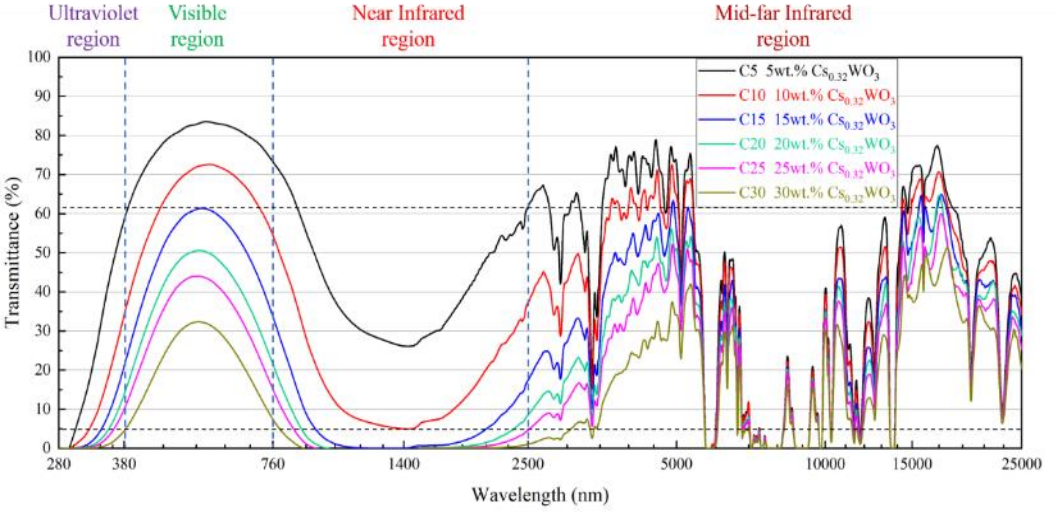

Fig. 15 The spectral transmittance curves of C5 ~ C30 $Cs_{0.32}WO_3$ thin film samples.

The UV-visible-NIR spectral transmittance of C5 ~ C30 $Cs_{0.32}WO_3$ thin film samples in 280 nm ~ 2500 nm band was measured by spectrophotometer, the mid-far infrared spectral transmittance of C5 ~ C30 $Cs_{0.32}WO_3$ thin film samples in 2.5 μm ~ 25 μm band was measured by Fourier infrared spectrometer. The spectral transmittance of C5 ~ C30 $Cs_{0.32}WO_3$ thin film samples in 280 nm ~ 25 μm band was composed by combining the two above-measured data, as shown in Fig. 15.

With the increase of $Cs_{0.32}WO_3$ content, the UV blocking rate B_{365nm} of the films continues to rise, from 64.4% of the C5 film sample to 99.6% of the C30 film sample, almost completely blocking UV. The visible transmittance T_{550nm} decreased from 83.8% of C5 film sample to 32.9% of C30 film sample. The solar near-infrared blocking rate continues to rise, and B_{940nm} rises from 53.0% of C5 film sample to 100% of C30 film sample, and B_{1400nm} rises faster than B_{940nm}, rising from 73.8% of C5 film sample to 99.9% of C15 film sample, almost completely blocking NIR. The transmittance changes in the mid-far infrared band have some differences in different bands, the transmittance in 2.5 μm ~ 5 μm band decreases rapidly, from about 70% of the C5 film sample to about 20% of the C30 film sample. While the transmittance in 5 μm ~ 25 μm band decreases slowly, the highest peak only decreased from about 70% of the C5 film sample to about 50% of the C30 film sample. The results show that $Cs_{0.32}WO_3$ films have a strong blocking effect in the ultraviolet and near-infrared bands, but have high transmittance in mid-far infrared bands. When the films are affixed to the inner surface of the glass window, the thermal radiation of the higher temperature glass can enter the room in large quantities in summer, and the thermal radiation of indoor higher temperature objects can pass through the films and be absorbed by the glass in large quantities in winter, both situations are not conducive to energy saving.

The UV-visible-NIR spectral reflectance of C5 ~ C30 $Cs_{0.32}WO_3$ thin film samples in 280 nm ~ 2500 nm band was measured by spectrophotometer, and the mid-far infrared spectral reflectance of C5 ~ C30 $Cs_{0.32}WO_3$ thin film samples

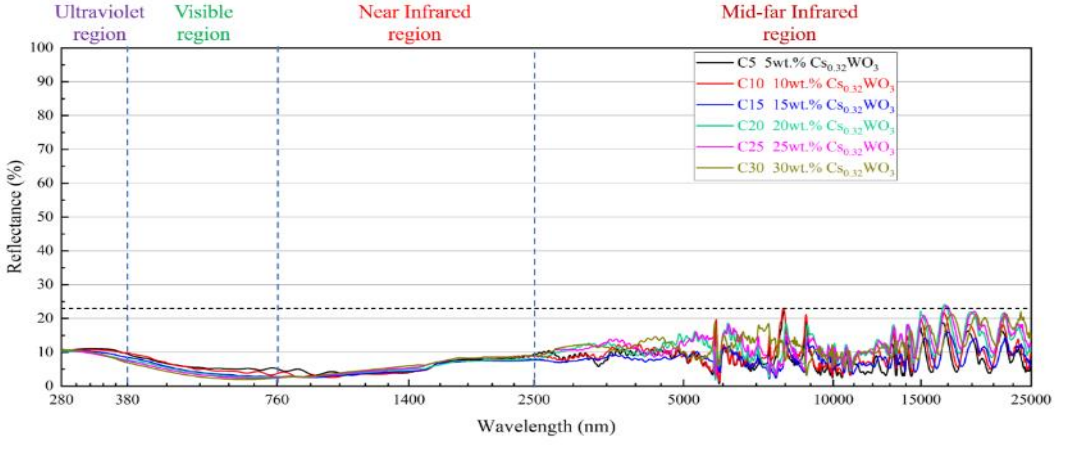

Fig. 16 The spectral reflectance curves of C5 ~ C30 $Cs_{0.32}WO_3$ film samples.

in 2.5 μm ~ 25 μm band was measured by Fourier infrared spectrometer. The spectral reflectance of C5 ~ C30 $Cs_{0.32}WO_3$ thin film samples in 280 nm ~ 25 μm band was composed by combining the two above-measured data, as shown in Fig. 16. As can be seen from the Fig. 16, the reflectance of the films in the whole band of 280 nm ~ 2500 nm is very low, which has no significant change and indicates that the $Cs_{0.32}WO_3$ content in the slurries has little effect on the reflectance of the films. In the UV band, the reflectance of the film decreases slightly with the increase of $Cs_{0.32}WO_3$ content, from about 10% of the C5 film sample to about 7% of the C30 film sample. The same is true in the visible light band, the reflectance only decreases from a maximum of about 9% of the C5 film sample to a maximum of about 7% of the C30 film sample. There was nearly no change in the NIR band, while the reflectance in the mid-far infrared band increases slowly with the increase of $Cs_{0.32}WO_3$ content, from the maximum of about 16% of the C5 film sample to the maximum of about 23% of the C5 film sample. The above results show that the $Cs_{0.32}WO_3$ films have a reflectance of less than 9% in the visible light band, which can well meet the requirements of architectural glass and automotive glass for visible light reflectance, but in the mid-far infrared band, the reflectance is below 23%. When the films are attached to the inner surface of the glass window, they cannot effectively reflect the thermal radiation of indoor objects with higher temperatures in winter , which is not conducive to energy saving.

Since the sum of the spectral transmittance, reflectance, and absorbance of one object is 1, the spectral absorbance of C5-C30 $Cs_{0.32}WO_3$ thin film samples in 280 nm ~ 25 μm band can be obtained from the measured spectral transmittance and reflectance data, as shown in Fig. 17.

It can be seen that with the increase of $Cs_{0.32}WO_3$ content, the UV absorbance A_{350nm} of the films continues to rise, from about 50% of the C5 film sample to about 90% of the C15 film sample, and then it basically remains stable. The visible light absorbance of the films increases significantly, A_{550nm} increases dramatically from about 11% of the C5 film sample to about 65% of the C30 film sample. The solar NIR absorbance increases continuously, and A_{940nm} increases from 54% of the C5 film sample to 97% of the C20 film sample, then remains stable. A_{1400nm} rises from 70% of the C5 film sample to 95% of the C15 film sample, and then it remains stable too. The absorbance in the mid-far infrared band has different changes in different bands. The absorbance in 2.5 μm ~ 5 μm band increases significantly, from about 20% of C5 film sample to about 70% of C30 film sample. In the band of 5 μm ~ 25 μm, the absorbance basically does not change with the increase of the $Cs_{0.32}WO_3$ content, while the absorbance in 7 μm ~ 14 μm atmospheric window band is up to 95%, indicating that the thermal radiation of higher temperature objects can be absorbed by the $Cs_{0.32}WO_3$ films in large amounts. The above results show that the $Cs_{0.32}WO_3$ films havehigh absorbance in both the solar radiation band and the mid-far infrared band, and the absorbance in the mid-far infrared band has little change with the increase of $Cs_{0.32}WO_3$ content. When the $Cs_{0.32}WO_3$ films are affixed to the inner surface of the glass window, the solar radiation and the thermal radiation of the higher temperature glass can be absorbed a lot by the films in summer, and the films will also substantially absorb the thermal radiation of indoor higher temperature objects in winter, then dissipate heat to the outside through the glass by heat transfer. In summary, the spectral absorbance characteristic of the $Cs_{0.32}WO_3$ film is not conducive to glass energy saving.

Based on the absorbance, transmittance, and reflectance

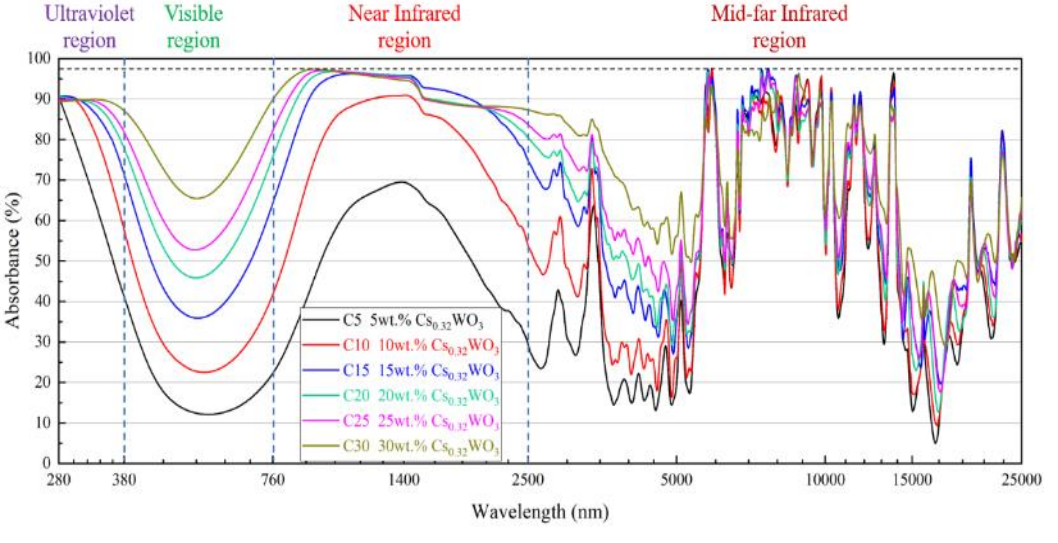

Fig. 17 The spectral absorbance curves of C5 ~ C30 $Cs_{0.32}WO_3$ film samples.

data of $Cs_{0.32}WO_3$, combined with the high emissivity and high mid-far infrared absorbance, the $Cs_{0.32}WO_3$ films in their current form are not suitable for general energy-saving applications in both summer and winter. As in summer, it would absorb solar radiation and emit heat back, while in winter, it would absorb heat from the indoor but also emit heat outward. The performance of $Cs_{0.32}WO_3$ as an energy-saving application can be assessed after AgNWs doping.

3.4 Preparation and characterization of $Cs_{0.32}WO_3$ thin films doped with AgNWs and other film samples for performance testing experiments

In recent experiments, when the $Cs_{0.32}WO_3$ slurries were mixed with 1 wt.% AgNWs, the emissivity of prepared films were all lower than 0.35, while the change of $Cs_{0.32}WO_3$ content in $Cs_{0.32}WO_3$ slurries had little effect on it. This fact means that the AgNWs content dominates the emissivity change of $Cs_{0.32}WO_3$ films. However, doping AgNWs will change the visible transmittance of the $Cs_{0.32}WO_3$ films, while the properties of the films should be compared at the same transmittance. In order to determine the comprehensive energy-saving changes of the $Cs_{0.32}WO_3$ films when doping AgNWs, this section plans to prepare some film samples with different visible transmittance for carrying out performance testing experiments to verify the calculated and analytic results.

As shown in Table 1, eight kinds of film samples were prepared and numbered. 5 pieces of each film sample were prepared, while 4 pieces match the size of 192 mm × 172 mm, used to be affixed to the four peripheral surfaces of the glass hut. One piece matches the size of 172 mm × 172 mm, corresponding to the roof surface of the glass hut. In these samples, the surface emissivity of the double-sided coating samples T70-4 and T60-4 should be basically equal to that of the $Cs_{0.32}WO_3$ films T70-3 and T60-3 doped with 1 wt.% AgNWs and both should be lower than 0.35, which is convenient for subsequent comparative testing.

The film samples were placed on a hot table at 70 ℃, and the surface emissivity of them was measured by the infrared thermal imager. Black tape with an emissivity of 0.95 was used as a reference. Visible light and infrared images were shown in Figs. S2 and S3.

It can be seen from the figures that the emissivity of the $Cs_{0.32}WO_3$ films in blue color (T70-2, T60-2) is as high as 0.87 and 0.88 respectively. Doped with AgNWs, the emissivity of the $Cs_{0.32}WO_3$ films (T70-3, T60-3) can be reduced to 0.31 and 0.33 respectively, and the color becomes lighter significantly. The emissivity of the double-sided coating films (T70-4, T60-4) is nearly equal to that of the T70-3, T60-3 films, but the color is darker than that of T70-3, T60-3 films. The Low-E films (T70-1, T60-1) have the lowest emissivity, less than 0.2, but the color is light gray-green, resulting in poor visual comfort.

In order to make a clear contrast between the non-doped $Cs_{0.32}WO_3$ films and the $Cs_{0.32}WO_3$ films doped with AgNWs, optical images of T70-2, T70-3, T60-2, and T60-3 were carried out by a triple metallographic microscope, as shown in Fig. 18. It can be observed that, at the same transmittance of T550nm, dense AgNWs network structures are formed in the films after doping with AgNWs, resulting in an emissivity lower than 0.35. However, the content of $Cs_{0.32}WO_3$ nanoparticles is significantly reduced compared with that of

Table 1. The information sheet of film samples for the performance testing experiments.

Sample Number	T_{550nm}	Sample description	Method of preparation
T70-1	70%	Low-E thin film	Lab-made Low-E paint
T70-2	70%	$Cs_{0.32}WO_3$ thin film	slurry containing 11.4 wt.% $Cs_{0.32}WO_3$
T70-3	70%	$Cs_{0.32}WO_3$ thin film doped with AgNWs	The slurry containing 10.2 wt.% $Cs_{0.32}WO_3$ mixed with AgNWs slurry (solid content, 1.3 wt.%) at 1:3 ratio
T70-4	70%	Double-sided coating thin film	Coat the Low-E paint on the front of thin film and the slurry containing 5 wt.% $Cs_{0.32}WO_3$ on the back
T60-1	60%	Low-E thin film	Lab-made Low-E paint
T60-2	60%	$Cs_{0.32}WO_3$ thin film	slurry containing 15.6 wt.% $Cs_{0.32}WO_3$
T60-3	60%	$Cs_{0.32}WO_3$ thin film doped with AgNWs	The slurry containing 26.5 wt.% $Cs_{0.32}WO_3$ mixed with AgNWs slurry (solid content, 1.3 wt.%) at 1:3 ratio
T60-4	60%	Double-sided coating thin film	Coat the Low-E paint on the front of thin film and the slurry containing 10 wt.% $Cs_{0.32}WO_3$ on the back

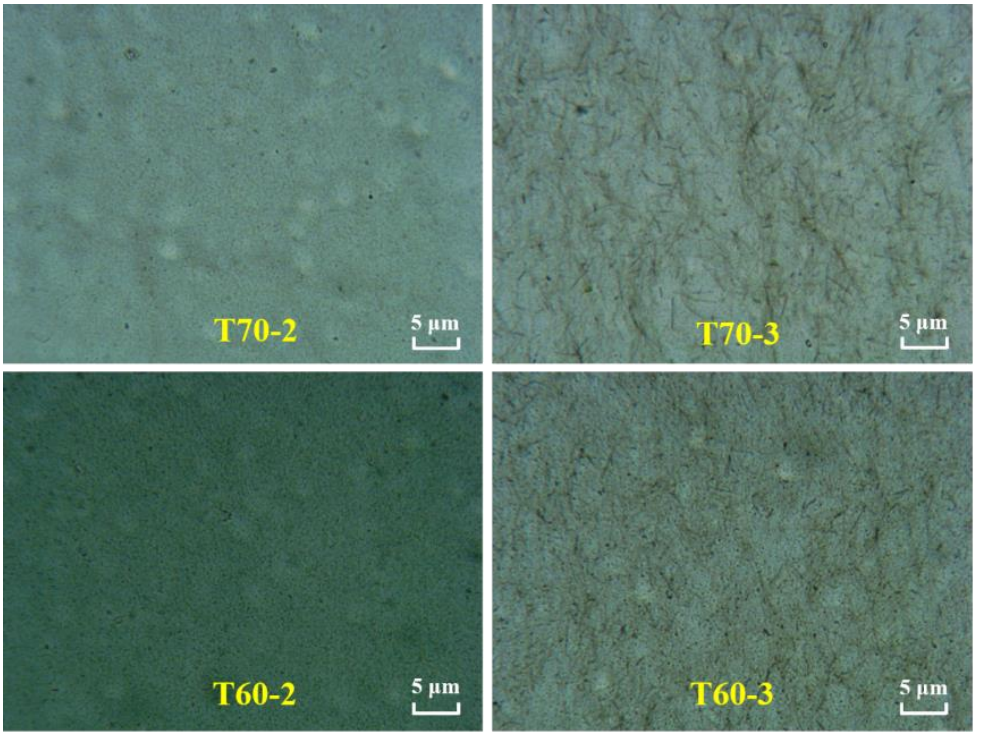

Fig. 18 The optical images of T70-2, T70-3, T60-2, and T60-3 film samples.

the non-doped $Cs_{0.32}WO_3$ films, which will undoubtedly affect the spectral characteristics of the films in the solar radiation band.

The spectral transmittance of the film samples in 280 nm ~ 25 μm band measured by spectrophotometer and Fourier infrared spectrometer is shown in Figs. 19 and 20, and the spectral reflectance is shown in Figs. 21 and 22. The spectral absorbance can be calculated according to the sum of transmittance, reflectance and absorptivity is 1, as shown in Figs. 23 and 24.

To more accurately compare the performance of each film sample and determine the comprehensive energy-saving effect of the $Cs_{0.32}WO_3$ thin film doped with AgNWs, the main optical properties of the 8 thin film samples were calculated according to the description and formulae in Table 2, and the results were shown in Table 3.

It can be seen that the T_{550nm} of T70-1 ~ T70-4 samples are about 70%, with a maximum difference of 0.9%, and the T_{550nm} of T60-1 ~ T60-4 samples is about 60%, with a maximum difference of 0.7%, meeting the visible

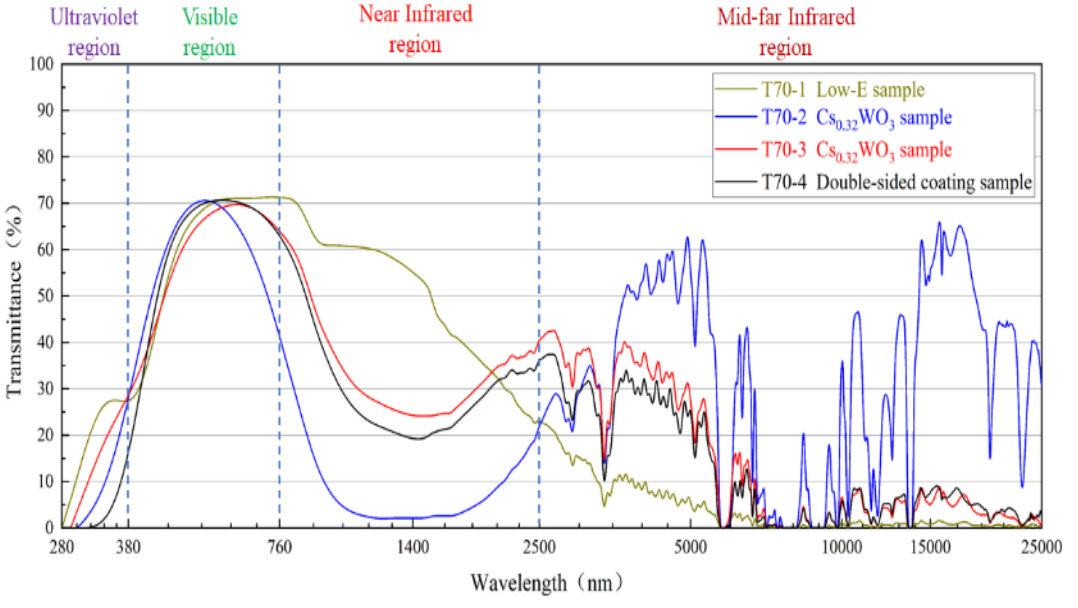

Fig. 19 The spectral transmittance curves of T70-1 ~ T70-4 film samples.

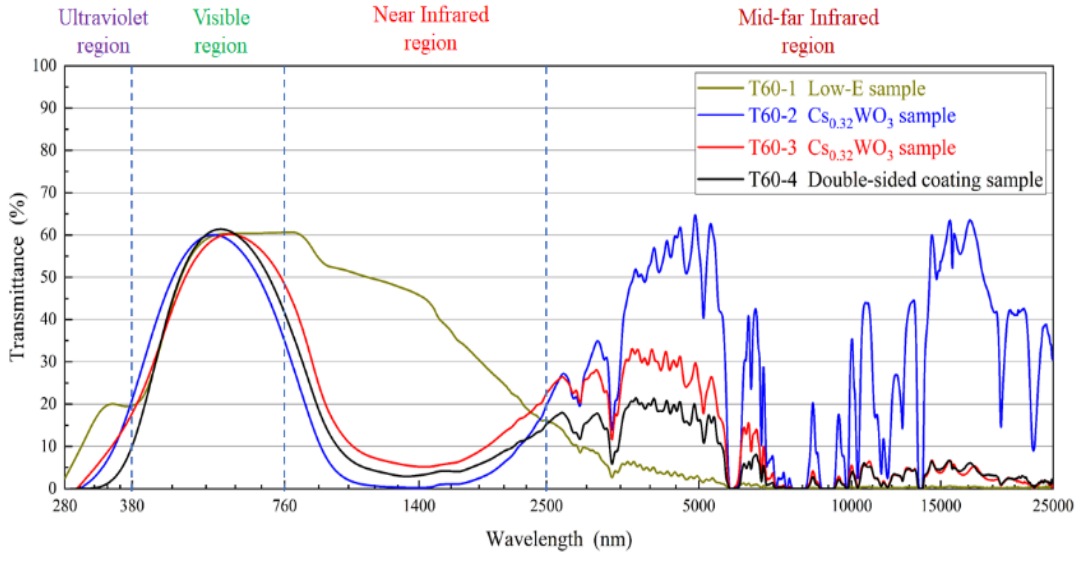

Fig. 20 The spectral transmittance curves of T60-1 ~ T60-4 film samples.

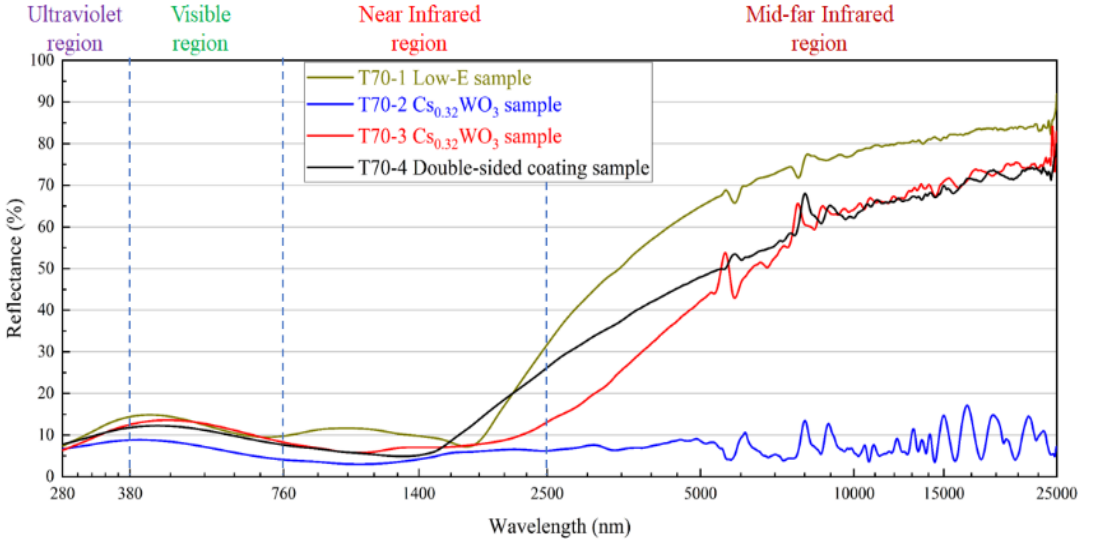

Fig. 21 The spectral reflectance curves of T70-1 ~ T70-4 film samples.

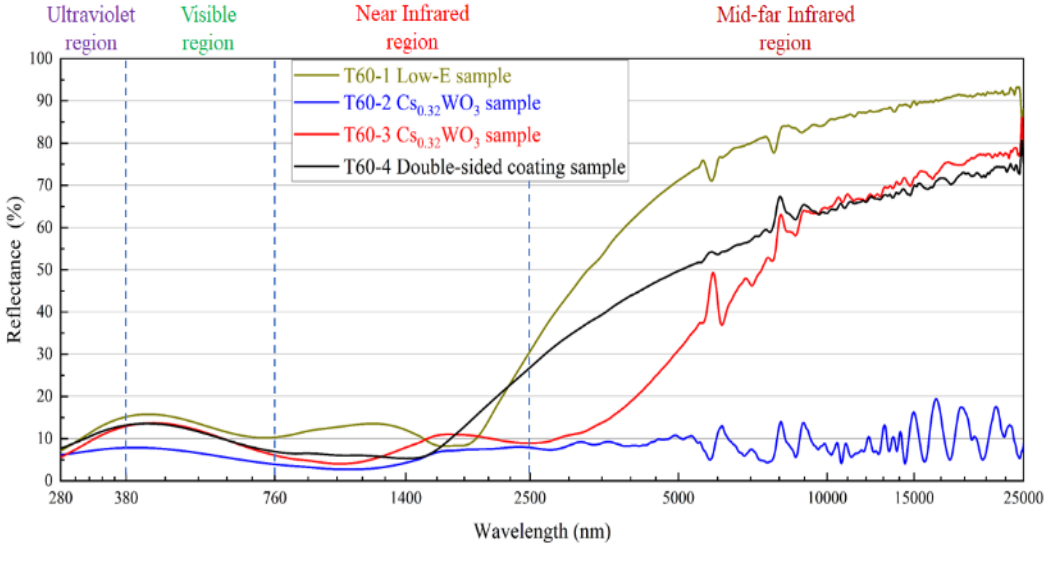

Fig. 22 The spectral reflectance curves of T60-1 ~ T60-4 film samples.

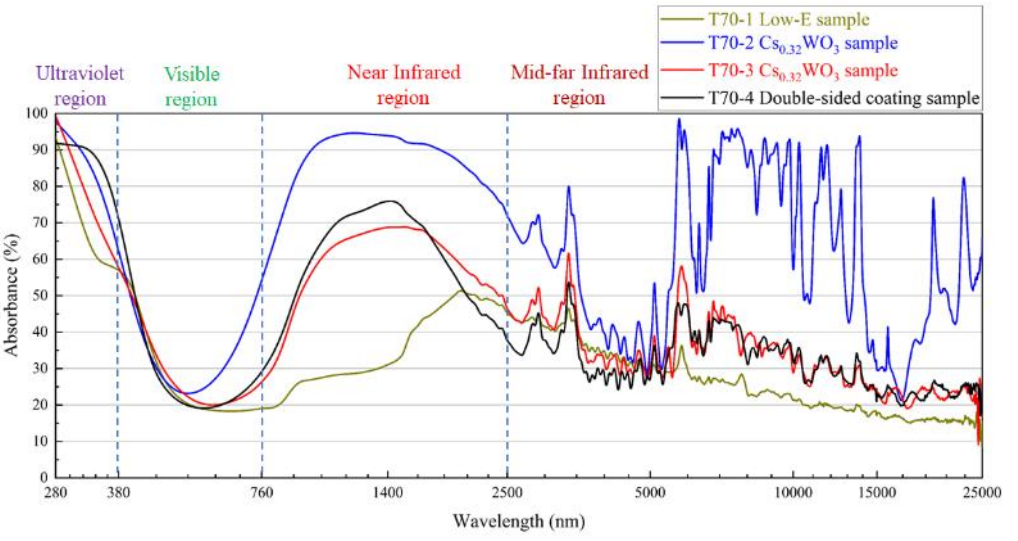

Fig. 23 The spectral absorbance curves of T70-1 ~ T70-4 film samples.

Table 2. Description and calculation of optical performance index of film samples.

Optical performance index	Definition and description	Data sources and calculations
T_{550nm}	Visible light transmittance of the sample at 550 nm	spectrophotometer
B_{365nm}	The UV blocking rate of the sample at 365 nm	spectrophotometer
B_{940nm}	The NIR blocking rate of the sample at 940 nm	spectrophotometer
B_{1400nm}	The NIR blocking rate of the sample at 1400 nm	spectrophotometer
T_s	The solar radiation transmittance of the sample	$T_s \approx \frac{\sum_{280}^{2500} S_\lambda \cdot T_\lambda \cdot \triangle_\lambda}{\sum_{280}^{2500} S_\lambda \cdot \triangle_\lambda}$
R_s	The solar radiation reflectance of the sample	$R_s \approx \frac{\sum_{280}^{2500} S_\lambda \cdot R_\lambda \cdot \triangle_\lambda}{\sum_{280}^{2500} S_\lambda \cdot \triangle_\lambda}$
A_s	The solar radiation absorbance of the sample	$R_s + T_s + A_s = 1$
S_λ	The solar spectral radiant intensity	The standard distribution of terrestrial solar spectral radiation
$\triangle_\lambda$	Wave difference	2 nm assigned in this paper
B_λ	The 300 K blackbody spectral radiant intensity	$B_\lambda = \frac{C_1 \lambda^{-5}}{e^{\frac{C_2}{\lambda T}} - 1}$ C_1: Planck's first constant 3.743×10^8 W·μm^4/m^2 C_2: Planck's second constant 1.439×10^4 μm·K
R_{MIR}	The Mid-far infrared reflectance of the sample in the band of 2.5 μm ~ 25 μm	$R_{MIR} \approx \frac{\sum_{2500}^{25000} B_\lambda \cdot R_\lambda \cdot \triangle_\lambda}{\sum_{2500}^{25000} B_\lambda \cdot \triangle_\lambda}$
T_{MIR}	The Mid-far infrared transmittance of the sample in the band of 2.5 μm ~ 25 μm	$T_{MIR} \approx \frac{\sum_{2500}^{25000} B_\lambda \cdot T_\lambda \cdot \triangle_\lambda}{\sum_{2500}^{25000} B_\lambda \cdot \triangle_\lambda}$
A_{MIR}	The Mid-far infrared absorbance of the sample in the band of 2.5 μm ~ 25 μm	$R_{MIR} + T_{MIR} + A_{MIR} = 1$
g	Total transmittance of solar energy	$g = T_s + N_i A_s$ $N_i = \frac{h_i}{h_i + h_o}$ $h_i = h_c + h_r = 3.6 + \frac{4.4\varepsilon_i}{\varepsilon_e}$

Optical performance index	Definition and description	Data sources and calculations
		$\varepsilon_i = \frac{1}{\frac{1}{\varepsilon_{surf}} + \frac{1}{\varepsilon_{in}} - 1}$
h_o	Composite convective heat transfer coefficient of outer surface	23 W/($m^2 \cdot K$) evaluated in this paper
ε_{surf}	The front emissivity of the sample	Infrared thermal imager
ε_{in}	Indoor ambient emissivity	0.9 evaluated in this paper
SC	Shading coefficient of the sample	$\mathrm{SC} = \frac{\mathrm{g}}{\tau}$
τ	The total solar transmittance of 3 mm thick ordinary glass	0.87

transmittance requirements of experimental comparison. The mid-far infrared transmittance T_{MIR} of T70-1 and T60-1 is less than 1%, and the reflectance R_{MIR} is as high as 78.8% and 86% respectively, but the NIR blocking rate $B_{1400\mathrm{nm}}$ is only 44.8% and 52.8%, much lower than other samples, which indicates a poor solar radiation blocking ability. While the NIR blocking rate of $Cs_{0.32}WO_3$ films T70-2 and T60-2 is the highest — the $B_{1400\mathrm{nm}}$ can reach 97.6% and 99.9% respectively showing a very strong solar radiation blocking ability, but the T_{MIR} can reach up to about 30%, the R_{MIR} is less than 10%, and the A_{MIR} exceeds 60%. When the $Cs_{0.32}WO_3$ films doped with AgNWs, the $B_{1400\mathrm{nm}}$ of T70-3 is 74.8% and the $B_{940\mathrm{nm}}$ is 59.2% showing a significant decrease compared with the T70-2 sample, which indicates a significant decline in the solar radiation blocking ability. While the $B_{1400\mathrm{nm}}$ of T60-3 is 94.8% and the $B_{940\mathrm{nm}}$ is 83.6%, showing a slight decrease compared with the T60-2 sample, which indicates a little decline in the solar radiation blocking ability. The T_{MIR} of T70-3 and T60-3 is lower than 5%, the R_{MIR} is significantly increased to more than 65%, and the A_{MIR} is below 30%, much less than T70-2, T60-2. The performance of double-sided coating films T70-4 and T60-4 is basically the same as that of T70-3 and T60-3. In addition, the shading coefficient (SC) value of T70-3 is 0.677, which is higher than that (0.625) of T70-2. While the SC value of T60-3 is 0.528, which is lower than that (0.540) of T60-2.

Table 4 data shows that in comparison to $T_{550\mathrm{nm}}$ equal to 70%, when $T_{550\mathrm{nm}}$ is 60%, doping AgNWs can not only improve the solar radiation blocking ability of $Cs_{0.32}WO_3$ thin films but also greatly improving the mid-far infrared reflective ability, thus improving the comprehensive energy-saving effect of $Cs_{0.32}WO_3$ thin films.

3.5 Performance testing experiment for simulating indoor heating in winter

The prepared film samples were affixed to the inner surfaces of the customized glass huts (the size: 180mm × 180mm × 200mm) with high transparent adhesive; the heating coils were placed on the inner seat equipped with a heat insulation pad. The probes of the air temperature sensors were placed 8 cm above the center of the wire coils, and the heating coils and temperature sensors were connected to the electric energy meters. The electric energy meters were set to start heating when the temperature in the huts was below 18 ℃ and to stop heating when the temperature in the huts was below 26 ℃. The humidity inside and outside the huts was between 10% and 55%, and then the power consumption was recorded every

Table 3. The summary of main optical properties of film samples in performance testing experiments.

Sample number	B_{365nm}	T_{550nm}	B_{940nm}	B_{1400nm}	T_{MIR}	R_{MIR}	A_{MIR}	ε_{surf}	SC
T70-1	68.9%	70.7%	39.1%	44.8%	0.8%	78.8%	20.4%	0.2	0.745
T70-2	86.8%	70.4%	91.4%	97.6%	30.5%	9.4%	60.1%	0.87	0.625
T70-3	77.4%	69.8%	59.2%	74.8%	4.4%	66.7%	28.9%	0.31	0.677
T70-4	98.0%	70.1%	63.3%	80.2%	4.6%	67.4%	28.0%	0.32	0.668
T60-1	77.8%	59.8%	45.8%	52.8%	0.4%	86.0%	13.6%	0.19	0.647
T60-2	94.7%	60.2%	95.0%	99.9%	29.2%	9.9%	60.9%	0.88	0.540
T60-3	89.8%	60.2%	83.6%	94.8%	4.2%	65.2%	30.6%	0.33	0.528
T60-4	98.0%	60.5%	86.2%	96.5%	4.1%	65.6%	30.3%	0.32	0.514

Table 4. The summary of result from main optical properties of film samples in performance testing experiments.

Sample number	Observations on Absorbance	Observations on Reflectance (R_{MIR})	Observations on Transmittance (T_{550nm})	Overall Conclusions
T70-1	Low in NIR	High (78.8%)	High (≈ 70%)	Low solar blocking effectiveness
T70-2	High in NIR (B1400nm ≈ 97.6%)	Low (< 10%)	High (≈ 70%)	Strong solar blocking but high mid-far infrared emission (TMIR ≈ 30%)
T70-3	Lower than T70-2 in NIR (B1400nm ≈ 74.8%)	Increased compared to T70-2 (> 65%)	Similar to T70-2 (≈ 70%)	Reduced mid-far infrared emission (TMIR < 5%) but potentially lower NIR blocking than T70-2
T70-4	Similar to T70-3	Similar to T70-3	Similar to T70-3	Similar to T70-3
T60-1	Low in NIR	High (≈ 86%)	High (≈ 60%)	Low solar blocking effectiveness
T60-2	High in NIR (B1400nm ≈ 99.9%)	Low (< 10%)	High (≈ 60%)	Strong solar blocking but high mid-far infrared emission (TMIR ≈ 30%)
T60-3	Lower than T60-2 in NIR (B1400nm ≈ 94.8%)	Increased compared to T60-2 (> 65%)	Similar to T60-2 (≈ 60%)	Reduced mid-far infrared emission (TMIR < 5%) decrease in NIR blocking compared to T60-2
T60-4	Similar to T60-3	Similar to T60-3	Similar to T60-3	Similar to T60-3

2 hours. The glass huts were placed on a windless, sunny day with a temperature range of -4 ℃ ~ 5 ℃ to simulate indoor heating in winter, as shown in Fig. S4. An ordinary glass hut model was used for reference comparison.

After 24-hour test, the changes of power consumption of each glass hut model were recorded, as shown in Figs. 25 and 26. Taking the full-day energy consumption of ordinary glass hut model as integer 1, the energy consumption of other glass hut models is converted to the ratio shown in Table 5.

It can be seen that the full-day energy consumption of the glass huts with $Cs_{0.32}WO_3$ films T70-2 and T60-2 is the highest among the eight glass hut models, however, it still decreased

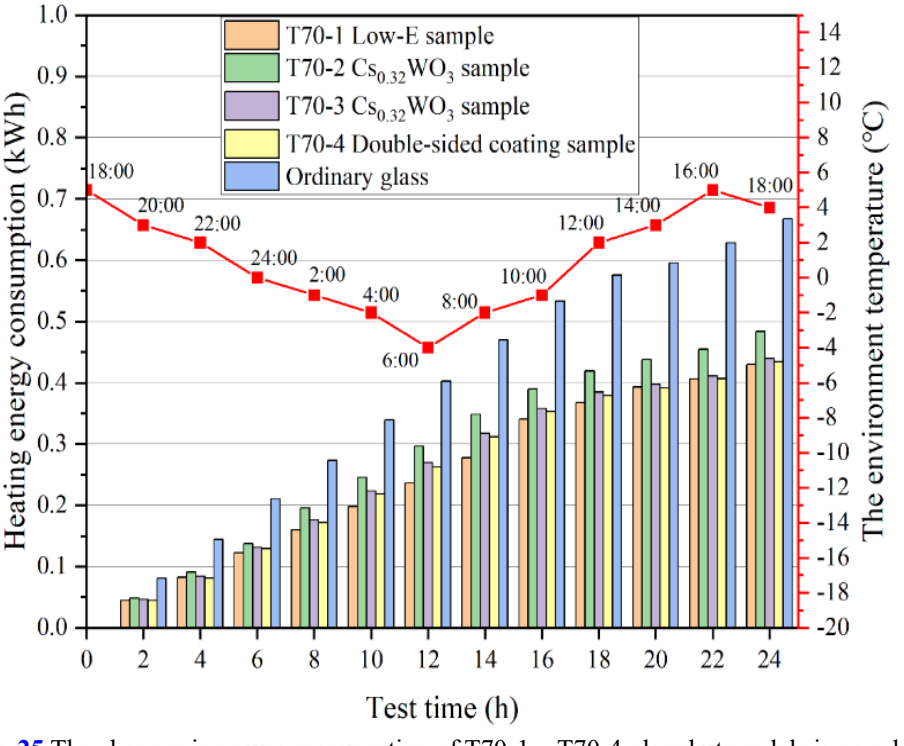

Fig. 25 The changes in power consumption of T70-1 ~ T70-4 glass hut models in one day.

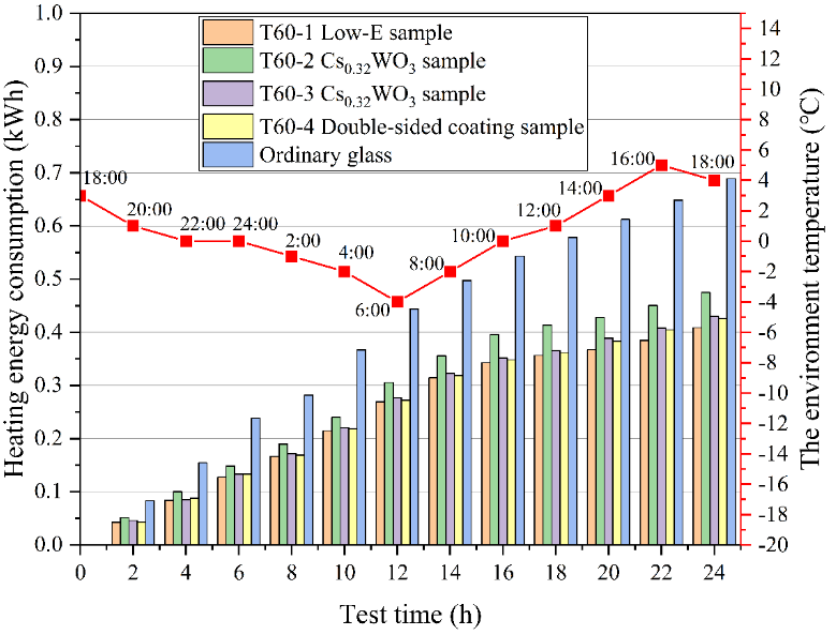

Fig. 26 The changes of power consumption of T60-1 ~ T60-4 glass hut models in one day.

Table 5. The ratio of energy consumption of different glass hut models to the ordinary glass hut.

Sample number	T70-1	T70-2	T70-3	T70-4	Ordinary glass hut
Energy consumption ratio	0.644	0.724	0.658	0.651	1
Sample number	T60-1	T60-2	T60-3	T60-4	Ordinary glass hut
Energy consumption ratio	0.593	0.689	0.624	0.618	1

by 27.6% and 31.1% respectively compared with the ordinary glass hut model, indicating that the $Cs_{0.32}WO_3$ films still have a certain energy-saving effect on indoor heating in winter, and the effect improves to some extent with the increase of $Cs_{0.32}WO_3$ content. The full-day energy consumption of the glass huts with $Cs_{0.32}WO_3$ films T70-3 and T60-3 doped with AgNWs was respectively 65.8% and 62.4% of that of the ordinary glass hut model, decreased by 9.1% and 9.4% respectively compared with that of the T70-2, T60-2 films, the full-day energy consumption of the glass huts with the two-sided coating films T70-4 and T60-4 was basically the same as that of T70-3 and T60-3 suggesting simple AgNWs doing will be more economical approach for winter energy saving applications. While the glass huts with the Low-E films T70-1, T60-1 gain the lowest full-day energy consumption - 64.4% and 59.3% respectively of that of the ordinary glass hut model, indicating that on the same conditions of T_{550nm}, Low-E films possess the best energy saving ability in winter among the 8 film samples.

The above results show that the energy saving ability of $Cs_{0.32}WO_3$ films in winter can be improved effectively when doped with AgNWs, on a par with the performance of the double-layer coating films. This finding provides compelling evidence for two fold benefits improving the spectral performance for winter application and simplifying the mass production process of $Cs_{0.32}WO_3$ films.

3.6 Performance testing experiment for simulating indoor warming in summer

This experiment was conducted in a sunny and windless afternoon in winter, when the outdoor temperature is 8 ℃. The dial thermometers were placed in the prepared glass hut models, with the orientation pointed directly to the sunshine to simulate the indoor warming in summer, as shown in Fig. S5, performance testing experiment for simulating indoor warming in summer. The temperature changes of the thermometers within 20 minutes were recorded every 3 minutes, as shown in Figs. 27 and 28. An ordinary glass hut model was used for reference comparison.

Observations reveal that the temperature of the thermometers in the ordinary glass hut rise in the most rapid increase, reaching 32 ℃ within 15 minutes and then stabilizing thereafter, indicates minimum solar blocking allowing heat to enter the hut and accumulate. The temperature of the thermometers in the glass huts with the Low-E films T70-1 and T60-1 can reach above 30 ℃, close to that of the ordinary glass hut, indicating that the Low-E films possess inadequate solar radiation blocking ability, and allow solar

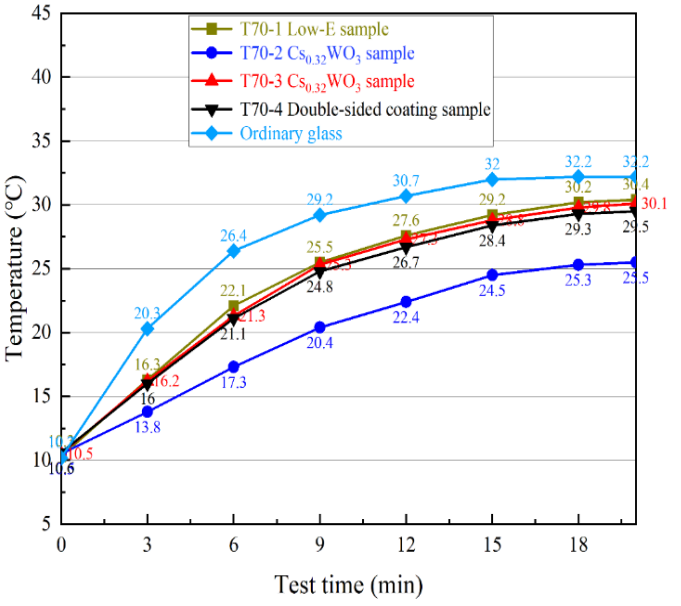

Fig. 27 Comparison of temperature rise in T70-1~T70-4 glass hut models.

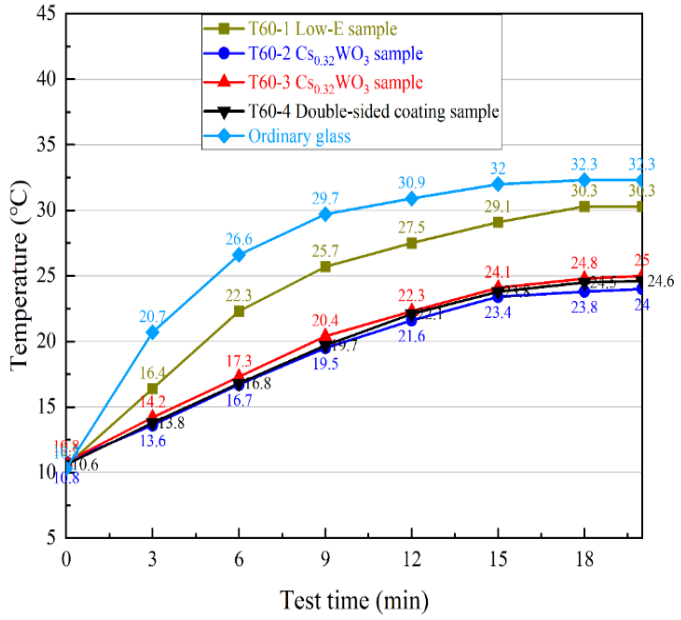

Fig. 28 Comparison of temperature rise in T60-1~T60-4 glass hut models.

radiation to pass through the films substantially, which can increase the temperature in the glass hut, meanwhile the indoor thermal radiation hardly gets dissipated due to the high mid-far infrared reflective ability of the Low-E films. This combined effect will lead to high temperature in the house and eventually result in a deficient energy saving effect in summer. In contrast the temperature of the thermometers in the T70-2 and T60-2 glass huts is 26 ℃ and 24 ℃ respectively, which is 6 ℃ and 8 ℃ lower respectively than that of the ordinary glass hut, indicating that the $Cs_{0.32}WO_3$ films have a strong solar radiation blocking ability and can significantly reduce the indoor temperature in summer. The temperature of the thermometer in the T70-3 glass hut rises to 30.1 ℃, showing a poor solar radiation blocking ability, while the temperature of the thermometer in the T60-3 glass hut rises to 25 ℃ — close to that of $Cs_{0.32}WO_3$ films, indicating that the $Cs_{0.32}WO_3$ film doped with AgNWs has a strong solar radiation blocking ability when the transmittance T_{550nm} is 60% and Thus make a good energy-saving effect in summer. Suggesting doping AgNWs might be more effective for films with lower visible light transmittance (T60) for summer applications. The temperature changes of the thermometers in the glass huts with double-sided coating films T70-4 and T60-4 are nearly the same as that of T70-3 and T60-3, suggesting minimum additional benefits of double-sided coating.

4. Conclusion

Based on the aforementioned experiments and analyses, it is evident that utilizing the solid-state reaction method, ball milling, and centrifugation, nano Cs_2CO_3 slurry (particle size less than 50 nm) can be prepared. However, the Cs_2CO_3 films exhibit an obvious high absorbance within the 280 nm ~ 25 μm wavelength range and high emissivity, which will cause a pronounced radiation heat exchange with the indoor environment during both summer and winter. The incorporation of AgNWs through doping enables the formation of a dense AgNWs network structure in the $Cs_{0.32}WO_3$ films, resulting in an emissivity of less than 0.35. When T_{550nm} is 70%, the $Cs_{0.32}WO_3$ film doped with AgNWs (mixing the $Cs_{0.32}WO_3$ slurry with AgNWs slurry (solid content, 1.3 wt.%) at 1:3 ratio) has better energy-saving effect in winter than the non-doped $Cs_{0.32}WO_3$ film because of its higher MIR reflectance, but the solar radiation blocking ability is poor, which results in few energy saving effect in summer. At a transmittance of 550 nm (T_{550nm}) of 60%, The $Cs_{0.32}WO_3$ film doped with 1 wt.% AgNWs not only have a better energy-saving effect in winter than that at T_{550nm} = 70 %, but also have a strong solar radiation blocking ability — approaching that of non-doped $Cs_{0.32}WO_3$ film. Although the solar radiation blocking ability of the $Cs_{0.32}WO_3$ film doped with AgNWs is not as strong as that of non-doped $Cs_{0.32}WO_3$ film, the much lower surface emissivity can significantly reduce the radiation heat transfer between the film and the room, which result in a lower shading coefficient (SC). Therefore, it achieves a commendable energy-saving effect comparable to that of the non-doped $Cs_{0.32}WO_3$ film during summer.

In summary, at a certain transmittance of 550 nm (T_{550nm}), for example, when T_{550nm} is 60%, the $Cs_{0.32}WO_3$ thin film doped with AgNWs can demonstrate superior solar radiation blocking ability ($B_{1400nm} > 94\%$) low emissivity ($\varepsilon_{surf} < 0.35$) and high mid-far infrared reflectance ($R_{MIR} > 65\%$). This configuration not only achieves a good energy-saving effect both in winter and summer, compensates for the deficiency observed in non-doped Cs0.32WO3 films, particularly their inadequate energy-saving performance during winter, but also provides meaningful technical reference and data support for further optimization research of $Cs_{0.32}WO_3$ film properties.

Acknowledgements
This work is supported by the National Key Research and Development Program of China (No. 2022YFB4602401), the Basic Science Center Program for Ordered Energy Conversion of the National Natural Science Foundation of China (No. 51888103, 51606192 and 52306018) and the CAS Pioneer Hundred Talents Program. Patents (CN 2024102620905, CN 202410262091X, CN 2024102620962 and CN 2024102620939) have been granted related to this work.

Conflict of Interest
There is no conflict of interest.

Supporting Information
Applicable.

References
[1] H. Sozer, Improving energy efficiency through the design of the building envelope, *Building and Environment*, 2010, **45**, 2581-2593, doi: 10.1016/j.buildenv.2010.05.004.
[2] H. Ye, X. Meng, L. Long, B. Xu, The route to a perfect window, *Renewable Energy*, 2013, **55**, 448-455, doi: 10.1016/j.renene.2013.01.003.
[3] Y. A. Eltbaakh, M. H. Ruslan, M. A. Alghoul, M. Y. Othman, K. Sopian, M. I. Fadhel, Measurement of total and spectral solar irradiance: overview of existing research, *Renewable and Sustainable Energy Reviews*, 2011, **15**, 1403-1426, doi: 10.1016/j.rser.2010.10.018.
[4] Y. Ozeki, T. Takabayashi, S.-I. Tanabe, Effects of spectral properties of glass on the thermal comfort of car occupants. *Elsevier Ergonomics Book Series*, 2005, 289-297, doi: 10.1016/s1572-347x(05)80047-3.
[5] B. Ingham, S. C. Hendy, S. V. Chong, J. L. Tallon, Density-functional studies of tungsten trioxide, tungsten bronzes, and related systems, *Physical Review B*, 2005, **72**, 075109, doi: 10.1103/physrevb.72.075109.
[6] K. A. Willets, R. P. Van Duyne, Localized surface plasmon resonance spectroscopy and sensing, *Annual Review of Physical Chemistry*, 2007, **58**, 267-297, doi: 10.1146/annurev.physchem.58.032806.104607.
[7] G. A. Niklasson, J. Klasson, E. Olsson, Polaron absorption in tungsten oxide nanoparticle aggregates, *Electrochimica Acta*, 2001, **46**, 1967-1971, doi: 10.1016/s0013-4686(01)00388-7.
[8] T. K. N. Nguyen, A. Renaud, M. Wilmet, N. Dumait, S. Paofai, B. Dierre, W. Chen, N. Ohashi, S. Cordier, F. Grasset, T. Uchikoshi, New ultra-violet and near-infrared blocking filters for energy saving applications: fabrication of tantalum metal atom cluster-based nanocomposite thin films by electrophoretic deposition, *Journal of Materials Chemistry C*, 2017, **5**, 10477-10484, doi: 10.1039/c7tc02454a.
[9] T. Abendroth, B. Schumm, S. A. Alajlan, A. M. Almogbel, G. Mäder, P. Härtel, H. Althues, S. Kaskel, Optical and thermal properties of transparent infrared blocking antimony doped tin oxide thin films, *Thin Solid Films*, 2017, **624**, 152-159, doi: 10.1016/j.tsf.2017.01.028.
[10] S. M. El-Bashir, I. S. Yahia, M. A. Binhussain, M. S. AlSalhi, Design of Rose Bengal/FTO optical thin film system as a novel nonlinear media for infrared blocking windows, *Results in Physics*, 2017, **7**, 1852-1858, doi: 10.1016/j.rinp.2017.05.027.
[11] C.-M. Wu, S. Naseem, M.-H. Chou, J.-H. Wang, Y.-Q. Jian, Recent advances in tungsten-oxide-based materials and their applications, *Frontiers in Materials*, 2019, **6**, 49, doi: 10.3389/fmats.2019.00049.
[12] C. Yang, J.-F. Chen, X. Zeng, D. Cheng, D. Cao, Design of the alkali-metal-doped WO_3 as a near-infrared shielding material for smart window, *Industrial & Engineering Chemistry Research*, 2014, **53**, 17981-17988, doi: 10.1021/ie503284x.
[13] Y. Yao, L. Zhang, Z. Chen, C. Cao, Y. Gao, H. Luo, Synthesis of Cs_xWO_3 nanoparticles and their NIR shielding properties, *Ceramics International*, 2018, **44**, 13469-13475, doi: 10.1016/j.ceramint.2018.04.158.
[14] A. Ghosh, Diffuse transmission dominant smart and advanced windows for less energy-hungry building: a review, *Journal of Building Engineering*, 2023, **64**, 105604, doi: 10.1016/j.jobe.2022.105604.
[15] X.-J. Huang, J. Bao, Y. Han, C.-W. Cui, J.-X. Wang, X.-F. Zeng, J.-F. Chen, Controllable synthesis and evolution mechanism of tungsten bronze nanocrystals with excellent optical performance for energy-saving glass, *Journal of Materials Chemistry C*, 2018, **6**, 7783-7789, doi: 10.1039/c8tc02740d.
[16] S. Yin, Y. Asakura, Recent research progress on mixed valence state tungsten based materials, *Tungsten*, 2019, **1**, 5-18, doi: 10.1007/s42864-019-00001-0.
[17] M. Mann, G. E. Shter, G. M. Reisner, G. S. Grader, Synthesis of tungsten bronze powder and determination of its composition, *Journal of Materials Science*, 2007, **42**, 1010-1018, doi: 10.1007/s10853-006-1384-x.
[18] P. Wang, T. Liu, S. Zhao, Z. Yang, Z. Ren, W. Jiang, X. Jiang, One-step ball-milling synthesis of cesium tungsten bronze nanoparticles and near-infrared shielding performance, *Ceramics International*, 2023, **49**, 21393-21401, doi: 10.1016/j.ceramint.2023.03.268.
[19] J. Guo, C. Dong, L. Yang, G. Fu, A green route for microwave synthesis of sodium tungsten bronzes NaxWO3, (0< x <1), *Journal of Solid State Chemistry*, 2005, **178**, 58-63, doi: 10.1016/j.jssc.2004.10.017.
[20] J. Wang, G. Tan, R. Yang, D. Zhao, Materials, structures, and devices for dynamic radiative cooling, *Cell Reports Physical Science*, 2022, **3**, 101198, doi: 10.1016/j.xcrp.2022.101198.
[21] G. Liu, F. Kong, J. Xu, R. Li, Novel synthesis of 0D, 1D and 2D nano-Cs_xWO_3 and their tunable optical-thermal response performance, *Journal of Materials Chemistry C*, 2020, **8**, 10342-10351, doi: 10.1039/d0tc01254h.
[22] M. C. Larciprete, A. Albertoni, A. Belardini, G. Leahu, R. Li Voti, F. Mura, C. Sibilia, I. Nefedov, I. V. Anoshkin, E. I. Kauppinen, A. G. Nasibulin, Infrared properties of randomly oriented silver nanowires, *Journal of Applied Physics*, 2012, **112**, 083503, doi: 10.1063/1.4759374.
[23] W. Li, H. Zhang, S. Shi, J. Xu, X. Qin, Q. He, K. Yang, W. Dai, G. Liu, Q. Zhou, H. Yu, S. R. P. Silva, M. Fahlman, Recent

progress in silver nanowire networks for flexible organic electronics, *Journal of Materials Chemistry C*, 2020, **8**, 4636-4674, doi: 10.1039/c9tc06865a.
[24] B. Shen, Development of advanced spectrally selective coating for the application of energy-efficient windows, 2022.
[25] R. Enneti, Synthesis of nanocrystalline tungsten and tungsten carbide powders in a single step via thermal plasma technique, *International Journal of Refractory Metals & Hard Materials*, 2015, **53**, 111-116, doi: 10.1016/J.IJRMHM.2015.06.011.